



# Hyperspectral near-infrared imaging for the detection of physical damages of pear



Wang-Hee Lee<sup>a</sup>, Moon S. Kim<sup>b</sup>, Hoonsoo Lee<sup>a</sup>, Stephen R. Delwiche<sup>c</sup>, Hanhong Bae<sup>d</sup>, Dae-Yong Kim<sup>a</sup>, Byoung-Kwan Cho<sup>a,\*</sup>

<sup>a</sup> Department of Biosystems Machinery Engineering, Chungnam National University, Daejeon 305-764, South Korea

<sup>b</sup> Environmental Microbial and Food Safety Laboratory, Agricultural Research Service, USDA, Beltsville, MD 20705, USA

<sup>c</sup> Food Quality Laboratory, Agricultural Research Service, USDA, Beltsville, MD 20705, USA

<sup>d</sup> School of Biotechnology, Yeungnam University, Gyeongsan 712-749, South Korea

## ARTICLE INFO

### Article history:

Received 23 August 2013

Received in revised form 26 December 2013

Accepted 30 December 2013

Available online 9 January 2014

### Keywords:

Hyperspectral imaging

F-value classification algorithm

Image processing

Near infrared spectrum

Pear bruise

## ABSTRACT

Bruise damage on pears is one of the most crucial internal quality factors, which needs to be detected in postharvest quality sorting processes. Near-infrared imaging techniques (NIR) have effective potentials for identifying and detecting bruises since bruises result in the rupture of internal cell walls due to defects on agricultural materials. In this study, a novel NIR technique, hyperspectral imaging with beyond NIR range of 950–1650 nm, was investigated for detecting bruise damages underneath the pear skin, which has never been examined in the past. A classification algorithm based on *F*-value was applied for analysis of image to find the optimal waveband ratio for the discrimination of bruises against sound surface. The result demonstrated that the best threshold waveband ratio detected bruises with the accuracy of 92%, illustrating that the hyperspectral infra-red imaging technique with the region beyond NIR could be a potential detection method for pear bruises.

© 2014 Elsevier Ltd. All rights reserved.

## 1. Introduction

Optical sensing and imaging technologies have been an effective tool for non-destructive inspection and assessment for quality and safety of agricultural/food products. For fruits, NIR spectral imaging is one of the most successful methods for detecting damages in the products, and recent advance in spectroscopic device allows developing innovative technique collecting information which cannot be obtained by conventional methods.

Recently, a novel method that integrates two mature technologies of imaging and spectroscopy, named hyperspectral image, has been developed and increasingly used for non-destructive evaluation of fruit quality. Hyperspectral sensing technique, also known as chemical imaging, collects image data at a series of narrow and contiguous wavelength bands, acquiring both spatial and spectral information simultaneously. The obtained data forms a three dimensional hyperspectral cube which consists of two dimensional spatial images with additional spectral information. The spectrum of each spatial pixel contains fingerprints or signatures of substances at corresponding spot on the hyperspectral image. As hyperspectral imaging can report both chemical and physical information of the material, it provides an opportunity for more

detail image analysis which makes it possible to discriminate either visually indistinguishable defects or spectrally similar materials. This novel technique was initially implemented for remote sensing applications which utilize satellite imaging data of planets such as mineral mapping (Clark et al., 1992), soil property detection (Ben-Dor et al., 2002), and vegetation mapping (Aber and Martin, 1995), but broaden its application to diverse fields of agriculture, pharmaceuticals and medical science.

Because hyperspectral imaging is applicable for large spatial sampling areas, it can be used for scanning the whole products, potentiating it as an effective tool for identifying and detecting spectral and spatial anomalies on agricultural products. Limitations of manual sorting and classical imaging technique, such as inefficiency, low accuracy, and labor and time-intensive nature, have launched the hyperspectral imaging in detecting fruit defects. Particularly, its high-sensitivity detecting indistinctive defects in agricultural products is fit for sensing bruise damage on fruits which deteriorates fruit quality, costing significant economic losses.

One of the earlier studies using NIR hyperspectral imaging technique was to investigate detection of bruises on Red Delicious and Golden Delicious apples (Lu, 2003). This study developed a suitable system for using an extended NIR range. It reports that reflectance of bruised damages increased over time in the spectral range between 1000 nm and 1340 nm corresponding to the most appropriate range for bruise detection with 54–94% of correct detection rate. Other researchers have also used hyperspectral image in the

\* Corresponding author. Address: 99 Deahak-ro(St.), Yuseong-gu, Daejeon 305-764, South Korea. Tel.: +82 42 821 6715; fax: +82 42 823 6246.

E-mail address: [chobk@cnu.ac.kr](mailto:chobk@cnu.ac.kr) (B.-K. Cho).

400–1000 nm region analyzed by statistical methods to detect bruises on 'Jonagold' apples after 1 day with an accuracy of 77.5% (Xing and De Baerdemaeker, 2005, 2007), and free formed bruises on 'Golden Delicious' with 86% accuracy (Xing et al., 2007). Similar application of hyperspectral imaging with the use of three NIR spectral bands at 750, 820, 960 nm was proposed for successful discrimination of bruised 'McIntosh' apples (ElMasry et al., 2008). Recently, 'Fuji' apples were studied using hyperspectral imaging technique to discriminate bruises with a classification threshold calculated by two-band ratio (Cho et al., 2011). Besides apples, damages on other fruits have been examined. Pits in tart cherries were optimally identified with spectral region between 692 and 856 nm in hyperspectral imaging (Qin and Lu, 2005), and a portable hyperspectral imaging device was utilized for detecting canker lesions on citrus fruit in the wavelength range between 400 and 900 nm (Qin et al., 2008). For detecting invisible bruises on 'Crystal' pears, four different classification algorithms were applied into hyperspectral image data collected with the spectral range of 408–1117 nm to compare classification accuracies (Zhao et al., 2010). Recent study on kiwifruit demonstrated that bruises on kiwifruit are detectable using 5 optimal wavelengths in the Vis/NIR hyperspectral image (Lu et al., 2011). Recently, a study has reviewed hyperspectral imaging technique in evaluating fruit and vegetable quality (Lorente et al., 2012).

It has been reported that internal quality of fruits is more effectively detected by an extended region beyond Vis/NIR (Lu et al., 2000; Moons et al., 1998). Nevertheless, few studies have been used NIR because of the lack of suitable NIR imaging devices covering the extended NIR region (Lu, 2003). Moreover, to our knowledge, only hyperspectral Vis/NIR imaging have been used to detect bruises on pears, but the extended range of NIR has not been used (Zhao et al., 2010), promoting the originality of this study using the extended range of NIR for pear bruise detection.

In this study, near infrared hyperspectral imaging in the 950–1650 nm region was firstly used to investigate the feasibility of multispectral reflectance ratio imaging techniques for detection of bruise damages on 'Shingo' pear. Simple ANOVA classification, a novel way to analyze hyperspectral imaging, was explored to select waveband ratio and threshold values for optimal classification of bruised pears (Cho et al., 2011). Findings in this study is expected to potentially propose developing low-cost and real-time multispectral imaging systems for quality sorting of pear in fruit processing plants.

## 2. Materials and methods

### 2.1. Fruits and bruising

'Shingo' pears were purchased from a local market in February 2011. For bruise treatments, two bruises spots in the middle area between stem and calyx on four individual pears were created by dropping the fruits. Three bruise levels were created using 5, 10 and 15 cm dropping heights. A total of 14 samples, four pears for each of three levels of bruise treatments, and two pears as control, were evaluated in this investigation. Hyperspectral images of pears were acquired before and after bruise treatments – measurements were conducted 1 h after the initial bruising, followed by 1, 2, 3, 4, 7, 9, and 11 days. For the duration of this hyperspectral imaging study, the sample pears were stored under ambient conditions (20 °C and 30% RH).

### 2.2. Hyperspectral imaging system

A schematic diagram of the hyperspectral NIR imaging system and form of three dimensional hyperspectral data are illustrated

in Fig. 1. It consists of a 320 (spatial) × 256 (spectral) pixel InGaAs Focal Plane Array (FPA) camera (Xenics, Model XEVA-1.7-320, 14-bit, Leuven, Belgium), an imaging spectrograph (SWIR Hyperspec, Headwall photonics, Fitchburg, MA, USA), and a 25-mm focal length lens (Optec, Model OB-SWIR25/2, Parabiago, Italy) along with a computer-controlled uniaxial stage (Velmex, Model XN10-0180-M02-21, Velmex Inc., Bloomfield, NY, USA). The spectrograph disperses incoming radiation from each spatial location on the line scan. The sample is scanned line-by-line over a nominal wavelength range of approximately 950–1650 nm. The use of a programmable positioning table allows line-by-line sample imaging for reflectance measurements. For each line scan measurement, the positioning table was incremented by 0.5 mm at an exposure time of 15 ms. The full hyperspectral image was acquired in about 110 s with 250 scans for a pear.

Illumination for reflectance imaging is provided by two 150 W quartz tungsten halogen lamps (Dolan Jenner, Model DC-950, MA, USA) and the lights are conveyed through low-OH fiber assemblies (1 m length, Dolan Jenner), with one end of the assembly coupled to the lamp enclosure and the other end arranged in a thin line (250 mm) of fibers. Two fiber assemblies are used to illuminate the line of IFOV (instantaneous field of view) of the imaging system, with the line of fibers positioned 75 mm above the IFOV at 10° forward and backward angle with respect to the vertical to illuminate the IFOV. Except for the QTH lamp box, imaging system

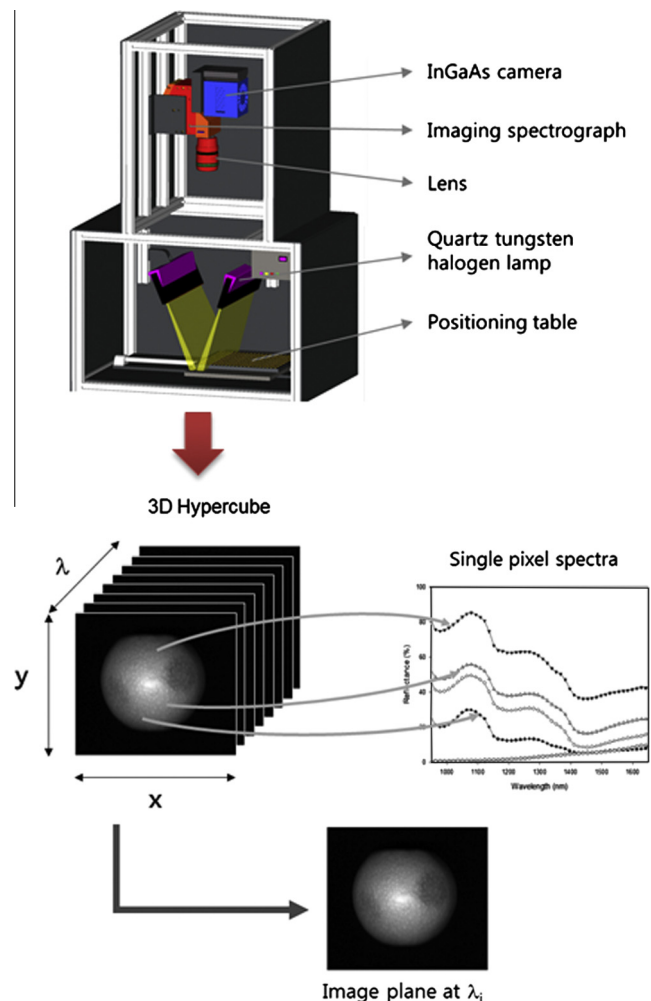


Fig. 1. Schematic illustration of NIR (950–1650 nm) hyperspectral reflectance imaging system and hypercube structure; spatial axes  $x$ ,  $y$ , and spectral axis  $\lambda$ .

is housed within an aluminum-framed enclosure with black foam board cladding. Fully-automated data acquisition interface software was developed using a Software Development Kit (SDK) provided by the camera manufacturers on a Microsoft (MS) Visual Basic (Version 6.0) platform in the MS Windows operating system.

### 2.3. Image parameters

In the spectral dimension,  $256 \times 30 \mu\text{m}$  pixels are available for the system. For the system with no vertical pixel binning, a total of 150 spectral pixels spanned the effective spectral imaging range from approximately 950 nm to 1650 nm, with a pixel-to-pixel wavelength separation of 4.82 nm.

Wavelength calibration for the system was conducted using a mixture of rare-earth oxides, dysprosium oxide ( $\text{Dy}_2\text{O}_3$ ), erbium oxide ( $\text{Er}_2\text{O}_3$ ), and holmium oxide ( $\text{Ho}_2\text{O}_3$ ), which exhibit many discrete absorption minima. The powder mixture, each oxide in equal weight, was lightly compacted to 0.5 cm thickness in a 3.5 cm diameter circular holder for measurement.

A white diffuse reflectance reference panel and dark current measurements were used to calculate percent reflectance values ( $R$ ).  $R$  for a spatial pixel ( $i$ ) at a given wavelength was calculated using the following equation:

$$R_i = \frac{RS_i - RD_i}{RR_i - RD_i} \times 100 \quad (1)$$

where  $RS$ ,  $RD$ , and  $RR$  are the raw intensity values of identical pixels from the sample image, dark current image, and white reference, respectively.

### 2.4. Image processing

This study focused on selecting a two-waveband ratio that could be applied toward developing low-cost and real-time imaging systems. In the two-waveband ratio, denominator played a role

for normalization of the spectra to minimize the outside intervention besides the reflectance of bruise and sound surface.

For comparing two groups of interest, a simple statistical comparison is sufficient tool for determining the significant difference between groups (Kutner, 2005). Selection was determined based on  $F$ -values of ANOVA between bruises and sound areas because our focus was to find an optimal waveband ratio for classifying those two areas. Following the waveband selection, frequency of all the waveband ratios for bruises and sound surfaces were recorded. Then, the optimal global threshold was determined at the point of the highest classification accuracy where the two frequency distributions were crossed. Spectra from individual pixels from the bruise and sound region of interests (ROI) were used in determining the optimal wavebands and threshold values (Cho et al., 2009).

MATLAB software (version 7.0.4, The Mathworks, Natick, MA) was used to process and analyze hyperspectral images.

### 3. Results and discussion

Representative spectra, extracted from NIR hyperspectral image of a pear including the bruises, sound areas, lenticels and regions with specular responses were measured with respect to wavelength (Fig. 2). Fig. 2(a) showed that original (left) and normalized hyperspectral images (right) of pear. As shown in the original image reflectance intensity variations of pear surfaces, especially from the center portion to the edges, were high because of round geometric shapes of the samples. To neutralize the effect of the round geometry of the fruits, the hyperspectral image data were normalized with respect to the peak values of individual spectra (bruise, sound surface, specular, and lenticel) achieved at around 1074 nm (Fig. 2(b)).

In the spectra, the dominant water absorption features (valleys) were observed at around 970 nm, 1190 nm, and 1450 nm, corresponding to absorption maxima of water in the NIR region (Bünning-Pfaue, 2003; Zheng et al., 2008). In general, relative reflectance

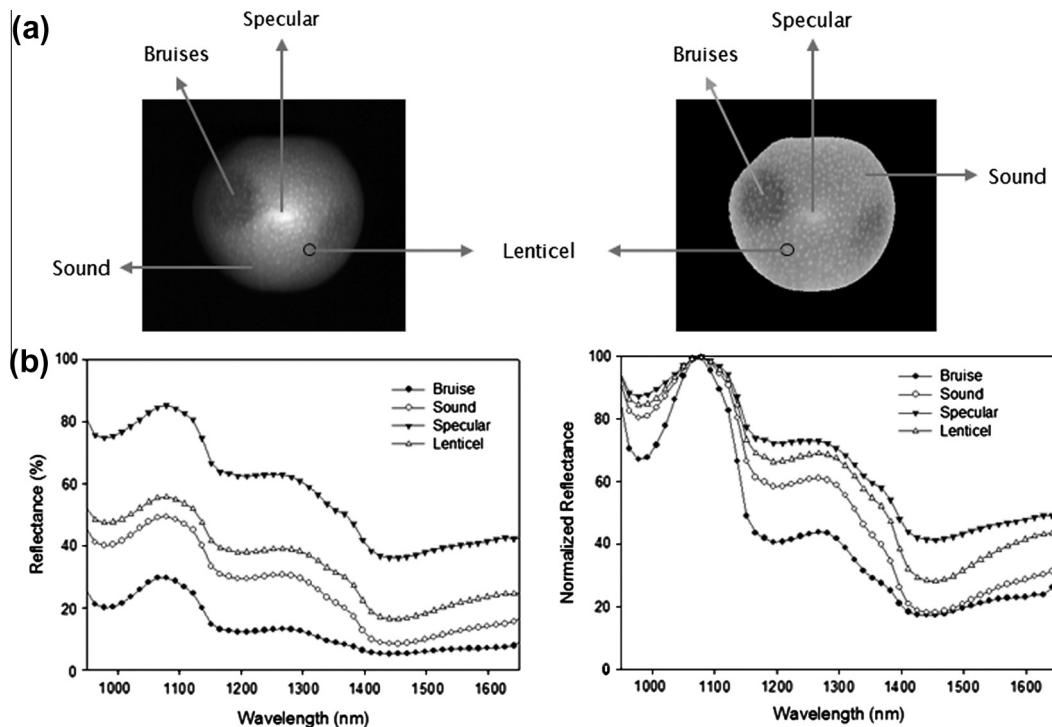


Fig. 2. Representative (a) spectral image (1200 nm) and (b) mean spectra of bruised and sound regions of pears before (left) and after (right) spectral normalization.

tance values of bruise regions are lower than those of other surface regions, suggesting that defects were detectable by water absorptive characteristics in the spectra. However, bruise regions from the normal pear surfaces cannot be easily differentiated with the use of a single spectral band image due to the high spatial variations. Normalization was able to circumvent this problem, and clarify that bruised regions exhibited relatively stronger water absorption compared to the sound regions. The images in Fig. 2 showed representative sample pear with two bruise spot at 1200 nm before and after the spectral normalization. These images confirmed the advantage of normalization. Compared to the unprocessed image, the normalized pear image in the lower clearly shows distinct compartmentalization of bruises caused by the relatively lower intensities of the bruised regions than the surrounding normal regions. In addition, the regions with specular responses were also reduced, minimizing the variations extrinsic to bruise detection. Consequently, the bruises areas in the normalized image could be more clearly identified than those in the original image. This observation suggested that bruises detection might be feasible with the use of two spectral bands in the NIR region under investigation; one for normalizing the spectra and the other for optimally detecting the bruises in the hyperspectral image. The selection of two bands effective for bruise detection was then performed, described in the following.

*F*-values of one-way ANOVA for all possible two wavebands ratio for the spectra of the two groups, bruises and sound areas were calculated to find the best waveband ratio pair for discriminating bruises from the sound surfaces of the entire hyperspectral images of pears before and after bruise treatments ( $n = 126$ ). A larger *F*-value indicates a more statistically significant mean separation between the two groups. Because of numerous ANOVA tables resulted from all the pair of two bands we used a contour plot for effectively reporting *F*-values. Fig. 3 showed that the most effective spectral wave lengths for discriminating bruises and sound surface, illustrated by contour plot. Contour image was plotted by *F*-values obtained from ANOVA for the bruises and sound surface groups of pears. The result showed that the means of the two groups were most significantly different (separated) by a two-band ratio at 1016 nm and 1074 nm wavelengths (R1074/R1016) indicated by white arrows in Fig. 3. Bruising involves chemical changes resulted from local degradation of the tissue combined with intracellular water exit and browning by oxidation of phenolic compounds from

released intracellular water (Pajuelo et al., 2003). However, 1016 nm and 1074 nm are not related to any of water and phenolic compounds, meaning that those bands are statistically significant in terms of discriminating bruise region from other areas using spectral image but not chemically interpretable. Similarly, Kamruzzaman et al. (2011) discriminated 3 types of lamb muscles. Waveband of 1074 nm was one of the main spectra for the muscle discrimination, but no chemical interpretation was assigned to 1074 nm, suggesting some waveband is effective for sensing, but chemically insignificant. An additional analysis for discovering chemical compounds matching to 1016 nm and 1074 nm may be interesting future subject.

In Fig. 4, where both distributions are crossed is the optimal threshold because it simultaneously minimizes erroneous classifications of bruises into sound surfaces or *vice versa*. For example, a ratio below the threshold increases misclassification of bruises to sound surface, while a larger ratio increases erroneous assignments of sound surface into bruises. To strictly determine the threshold, frequency distributions of appearance of two-waveband ratio for bruises and sound surfaces were individually regressed using Gaussian distribution (Eq. (2)).

$$Y(\text{frequency}) = \frac{1}{\sigma\sqrt{2\pi}} e^{-\frac{(x-\mu)^2}{2\sigma^2}} \quad (2)$$

where  $\mu$  is the mean of the ratio distributions (1.15 for bruises and 1.23 for sound surface), and  $\sigma$  is the standard deviation of the ratio distributions (0.0234 for bruises and 0.0368 for sound surface).  $x$  is the band ratio resulting in the corresponding frequency.

Then, the regression curves for bruises and sound surfaces were subtracted to find the zero-difference point, corresponding to the ratio of 1.19 (Eq. (3)).

$$\frac{1}{\sqrt{2\pi}} \left[ \frac{1}{\sigma_1} e^{-\frac{(x-\mu_1)^2}{2\sigma_1^2}} - \frac{1}{\sigma_2} e^{-\frac{(x-\mu_2)^2}{2\sigma_2^2}} \right] = 0 \quad (3)$$

where  $\mu_1 = 1.15$  and  $\mu_2 = 1.23$  which are the means of bruise and sound surface distributions, respectively, while standard deviations are  $\sigma_1 = 0.0234$  and  $\sigma_2 = 0.0368$ .

To confirm our analysis, classification accuracy for bruise from normal surfaces was then calculated for each a specific range of the band ratio value. The accuracy was determined by the number of pixels properly classified with comparing the ratio at the corresponding pixel to the threshold value (Cho et al., 2011). The highest classification accuracy (=92%) was observed at the consistent optimal threshold calculated by the distributions.

The *F*-value method is a novel algorithm which has been rarely used (Cho et al., 2011). Despite the method is relatively simple only requiring a basic statistics, it informs valuable result to find the optimal waveband for detecting bruises because numerical size of *F*-value directly indicates the significance. As the accuracy is pixel-based, this *F*-value method is adequate to distinguish the bruises with the sound surface on a sample rather than sample-based classification which tabulates the whole samples either as bruised or normal fruits. Moreover, with pixel-based classification, quantitative estimation of bruising area is possible and this may be applicable to evaluate the time after bruising or the scale of damage. Similarly, partial least square (PLS) classifies bruises based on pixels, and is effective for detecting early stage of bruising (ElMasry et al., 2008). However, previous apple study reported more than 50% of misclassification of bruises into sound area (Xing et al., 2007). In addition, PLS requires more complex mathematics than *F*-value method. Because of its simplicity, computational load and time of *F*-value method are low with comparable accuracy, suggesting the advantages of the *F*-value method on analyzing a large-size image data over complex statistical models. In classify-

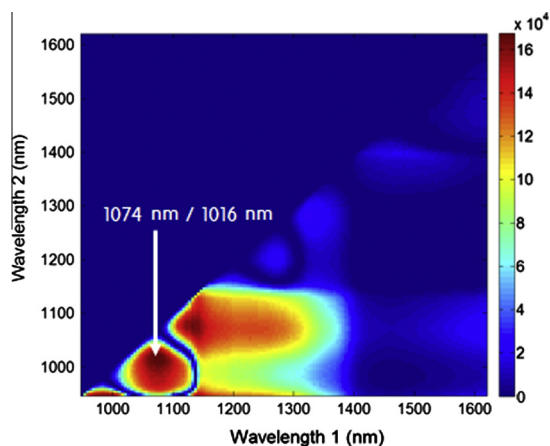


**Fig. 3.** Contour plot of *F*-value calculated by waveband ratio. The most effective wave length was searched and contour plot was built using *F* values for wavelength pairs (ratio) used for discriminating bruises from sound surface of pear. Color bar in the right-side of the contour plot shows *F*-value whose value increases from the blue to the red. (For interpretation of the references to color in this figure legend, the reader is referred to the web version of this article.)



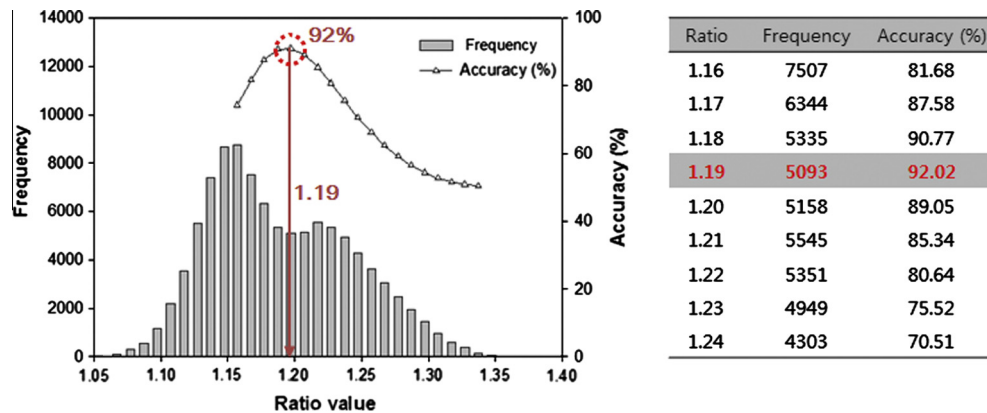


Fig. 4. Classification accuracy as a function of R1074 nm/R1016 band ratio threshold value with frequency histogram for ratio values of bruises and sound surfaces of pear.

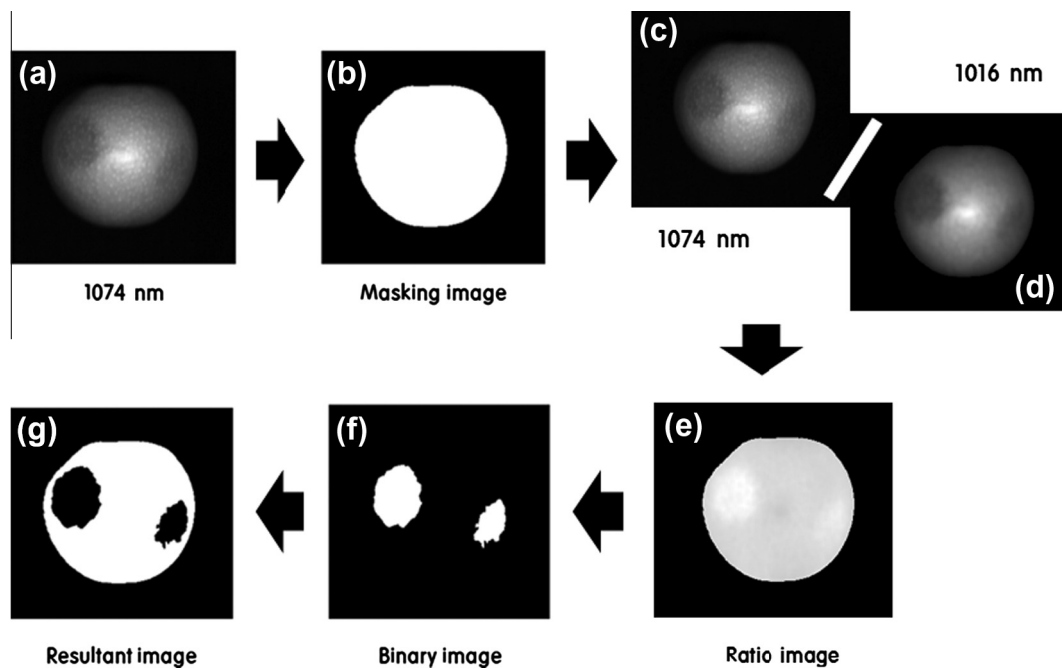


Fig. 5. Illustration of image processing sequences: (a) 1074 nm reflectance image; (b) binary mask image for pear surfaces obtained by applying a threshold of 10% reflectance to the 1074 nm image; (c) 1074 nm and (d) 1016 nm images, (e) two-waveband ratio (R1074/R1016) image, (f) bruised area determined by applying the threshold value of 1.19 to the R1074/R1016 image, and (g) resultant binary image showing the bruise region on the pear surfaces.

ing the whole unknown samples, unsupervised algorithm has been utilized. In the most sample-based studies, PCA has been the main analytical tool, informing effective wavebands for detecting bruised fruits from the total sampling pool (Lu et al., 2011; Lu, 2003; Qin et al., 2008; Xing and De Baerdemaeker, 2005, 2007). However, the accuracy was variable and relatively lower than other classifying algorithm, while an algorithm with high accuracy requires more complicate programming than PCA (Xing et al., 2007; Zhao et al., 2010). Finally, it should be noted that the *F*-value is only meaningful when comparing two areas. For detecting multiple regions, different algorithms such as multiple comparison and PCA are appropriate.

Compared to our previous study using *F*-value for selection of the optimal waveband ratio, this study resulted in higher accuracy (Cho et al., 2011). This may be because that the current study used beyond NIR region that partially includes SWIR (Short Wave Infra-Red) range. NIR has been used in most previous researches regarding fruit bruise detection. However, SWIR has shown relatively

higher accuracy in bruise classification for apples (Lu, 2003), consistent with the report that highlighted effective detection of quality of fruits by an extended region beyond Vis/NIR (Lu et al., 2000; Moons et al., 1998). Further investigations are necessary to prove the advantages of SWIR over NIR in detecting fruit bruises, particularly with respect to the varieties of fruits.

Fig. 5 illustrates a sequence of image processing procedures using the selected two-band ratio and threshold for classifying the bruise spots on the sample pear. Fig. 5(c) and (d) are 1074 nm and 1016 nm images, respectively, after the applications of pear surface area masking. The mask image for the pear surfaces in Fig. 5(b) was obtained by applying a threshold of 10% reflectance to the 1074 nm image, while Fig. 5(e) is a R1074/R1016 band ratio image, resulting from dividing the reflectance intensity at 1074 nm by that at 1016 nm. Fig. 5(f) is the binary-classification image where the optimum threshold value (1.19) was applied to the R1074/R1016 band ratio image. The resultant image clearly displays the bruised areas on the pear.

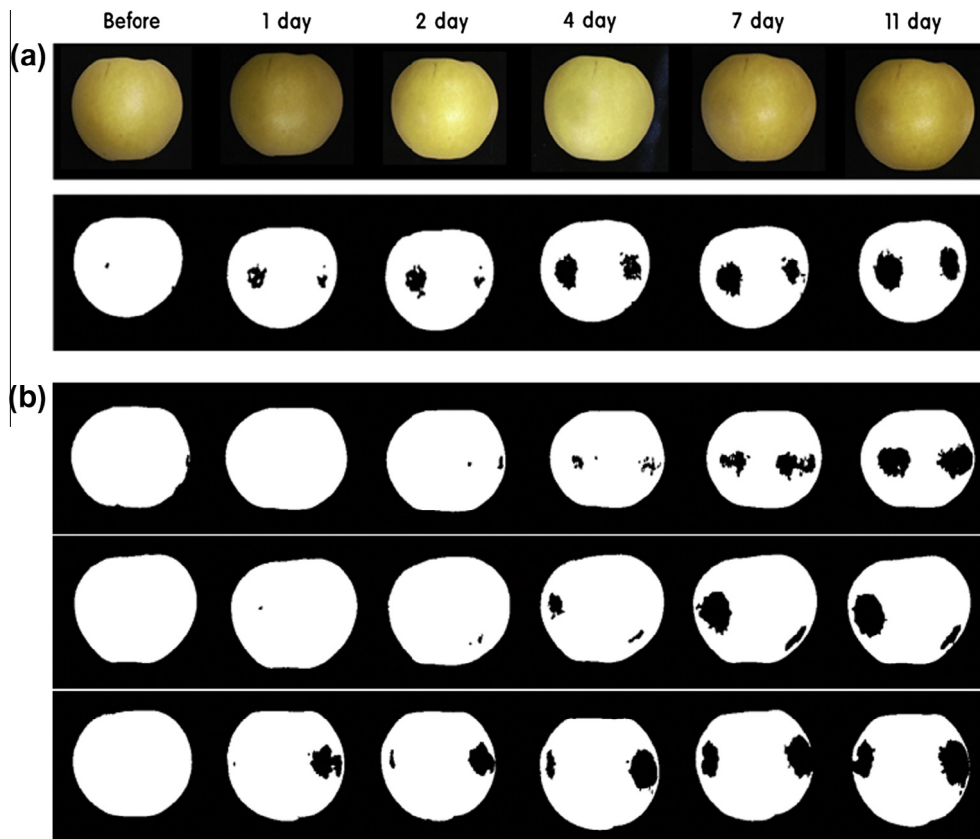


**Fig. 6.** Representative photos of (a) sample pear before and after bruising in 1, 2, 4, 7, 11 days and resultant ratio ( $R_{1074}/R_{1016}$ ) images, and (b) other sample images processed by  $F$ -value ratio method, validating the ability of the determined two band ratio for separating bruise and sound surface.

Fig. 6 shows a sequence of photos and processed images with respect to storing time after bruising. The bruised areas in the photos are hardly observed with visual inspection while distinctive regions of the bruise damage could be observed with the two wavebands ratio method in Fig. 6(a), which was also observed in other samples (Fig. 6(b)). Most of the pixels in the sound areas were successfully eliminated; however a few false positive pixels were observed in the sound areas of the samples. This may have been emanated from pre-existing damage or other defects. In most cases, qualitative detection of bruises is fully covered by the  $F$ -value method owing to the size of bruising area that normally has a diameter larger than 1 cm (Cho et al., 2011).

Preliminary evaluation of the resultant images for entire pear samples under investigation including the three bruise levels (dropped at 5, 10, and 15 cm heights) show the evident bruise damages (figure not shown). Individual pears exhibited variations in response to the dropping heights as the resultant images did not clearly exhibited a trend in response to the degrees of bruising levels. However, bruises on the most pears can be detected in 4 days following the bruising regardless of the dropping heights.

There are a few interesting future tasks stems from this study. As aforementioned, it would be an interesting to directly compare SWIR to NIR for detection of bruises on pears and even on other varieties of fruits. Secondly, we can compare the  $F$ -value method to other widely used classification algorithms, and consider to orchestrate  $F$ -values method with unsupervised method as both PLS and PCA have used to detect apple bruises by ElMasry and his colleagues (2008). For example, a study has compared different pear bruise classification algorithms with NIR (Zhao et al., 2010), but no publication compares different types of classification algorithms with beyond NIR range, such as SWIR image data.

#### 4. Conclusions

This study highlighted the feasibility of hyperspectral/multi-spectral NIR reflectance imaging technique for detecting bruise damages on 'Shingo' pears, which has never been tried before. A simple  $F$ -value statistics was sufficient to find the optimal waveband ratio and threshold for maximizing the bruise detection accuracy. The selected optimal NIR reflectance image ratio (1074 nm and 1016 nm:  $R_{1074}/R_{1016}$ ) demonstrated its ability to detect bruised areas from sound surface on pears. Further studies on bruised tissues of varieties of pears with larger sample numbers and longer storage time need to be investigated to develop a complete bruise-detection system for pears. The wavebands explored in this study could be helpful for developing real-time multispectral systems for discriminating bruised fruits in fruit quality sorting plants.

#### Acknowledgement

This work was partially supported by the Technology Commercialization Support Program, Ministry of Agriculture, Food and Rural Affairs(MAFRA), Republic of Korea. It was also partially supported by a grant from the Next-Generation BioGreen 21 Program (Plant Molecular Breeding Center No. PJ009078), Rural Development Administration, Republic of Korea.

#### References

- Aber, J., Martin, M., 1995. High spectral resolution remote sensing of canopy chemistry. Summaries of the Fifth Annual JPL Airborne Geosciences Workshop 1, Airborne Earth Science Workshop. JPL Publication 95-4, pp. 1–4.

- Ben-Dor, E., Patkin, K., Banin, A., Karnieli, A., 2002. Mapping of several soil properties using DAIS-7915 hyperspectral scanner data – a case study over clayey soils in Israel. *Int. J. Remote Sens.* 23, 1043–1062.
- Büning-Pfaue, H., 2003. Analysis of water in food by near infrared spectroscopy. *Food Chem.* 82, 107–115.
- Cho, B., Baek, I., Lee, N., Mo, C., 2011. Study on bruise detection of ‘fuji’ apple using hyperspectral reflectance imagery. *J. Biosyst. Eng.* 36, 484–490.
- Cho, B., Kim, M.S., Chao, K., Lawrence, K., Park, B., Kim, K., 2009. Detection of fecal residue on poultry carcasses by laser-induced fluorescence imaging. *J. Food Sci.* 74, E154–E159.
- Clark, R., Swayze, G., Gallagher, A., 1992. Mapping the mineralogy and lithology of Canyonlands, Utah with imaging spectrometer data and the multiple spectral feature mapping algorithm. *Summaries of the Third Annual JPL Airborne Geosciences Workshop 1, AVIRIS Workshop. JPL Publication 92-14*, pp. 60–62.
- ElMasry, G., Wang, N., Vigneault, C., Qiao, J., ElSayed, A., 2008. Early detection of apple bruises on different background colors using hyperspectral imaging. *Lwt-Food Sci. Technol.* 41, 337–345.
- Kamruzzaman, M., ElMasry, G., Sun, D.-W., Allen, P., 2011. Application of NIR hyperspectral imaging for discrimination of lamb muscles. *J. Food Eng.* 104, 332–340.
- Kutner, M.H., 2005. *Applied Linear Statistical Models*. McGraw-Hill Irwin, Boston, USA.
- Lorente, D., Aleixos, N., Gomez-Sanchis, J., Cubero, S., Garcia-Navarrete, O.L., Blasco, J., 2012. Recent advances and applications of hyperspectral imaging for fruit and vegetable quality assessment. *Food Bioprocess Technol.* 5, 1121–1142.
- Lu, Q., Tang, M., Cai, J., Zhao, J., Vittayapadung, S., 2011. Vis/NIR hyperspectral imaging for detection of hidden bruises on kiwifruits. *Czech J. Food Sci.* 29, 595–602.
- Lu, R., 2003. Detection of bruises on apples using near-infrared hyperspectral imaging. *Trans. Am. Soc. Agri. Eng.* 46, 523–530.
- Lu, R., Guyer, D., Beaudry, R., 2000. Determination of firmness and sugar content of apples using NIR diffuse reflectance. *J. Texture Stud.* 31, 615–630.
- Moons, E., Sinnaeve, G., Dardenne, P., 1998. Non-destructive visible and NIR spectroscopy measurement for the determination of apple internal quality. In: *Proceedings of the XXV International Horticultural Congress. Part 7. Quality of Horticultural Products: Starting Material, Auxiliary Products, Quality Control*, 2–7 August 1998, Brussels, Belgium.
- Pajuelo, M., Baldwin, G., Rabal, H., Cap, N., Arizaga, R., Trivi, M., 2003. Bio-speckle assessment of bruising in fruits. *Opt. Lasers Eng.* 40, 13–24.
- Qin, J., Lu, R., 2005. Detection of pits in tart cherries by hyperspectral transmission imaging. *Trans. Am. Soc. Agri. Eng.* 48, 1963–1970.
- Qin, J., Burks, T., Kim, M., Chao, K., Ritenour, M., 2008. Citrus canker detection using hyperspectral reflectance imaging and PCA-based image classification method. *Sens. Instrum. Food Qual. Saf.* 2, 168–177.
- Xing, J., De Baerdemaeker, J., 2005. Bruise detection on ‘Jonagold’ apples using hyperspectral imaging. *Postharvest Biol. Technol.* 37, 152–162.
- Xing, J., De Baerdemaeker, J., 2007. Fresh bruise detection by predicting softening index of apple tissue using VIS/NIR spectroscopy. *Postharvest Biol. Technol.* 45, 176–183.
- Xing, J., Saeys, W., De Baerdemaeker, J., 2007. Combination of chemometric tools and image processing for bruise detection on apples. *Comput. Electron. Agri.* 56, 1–13.
- Zhao, J., Ouyang, Q., Chen, Q., Wang, J., 2010. Detection of bruise on pear by hyperspectral imaging sensor with different classification algorithms. *Sensor Letters* 8, 570–576.
- Zheng, Y., Lai, X., Bruun, S.W., Ipsen, H., Larsen, J.N., Løwenstein, H., Søndergaard, I., Jacobsen, S., 2008. Determination of moisture content of lyophilized allergen vaccines by NIR spectroscopy. *J. Pharm. Biomed. Anal.* 46, 592–596.